Tight-binding model for graphene π-bands from maximally localized Wannier functions

Jeil Jung and Allan H. MacDonald

Tight-binding model for graphene π-bands from maximally localized Wannier functions

Jeil Jung and Allan H. MacDonald

Department of Physics, University of Texas at Austin, USA

The electronic properties of graphene sheets are often understood by starting from a simple phenomenological π-band tight-binding models. We provide a perspective on these models that is based on a study of *ab initio* maximally localized Wannier wave functions (MLWF) centered at carbon sites. Hopping processes in graphene can be separated into inter-sublattice contributions responsible for band dispersion near the Dirac point, and intra-sublattice contributions responsible for electron-hole symmetry breaking. Both types of corrections to the simplest near-neighbor model can be experimentally relevant. We find that distant neighbor hopping parameters increase the ratio of the full π-band width to the Dirac point velocity and flatten bands along the *KM* Brillouin-zone edge. We propose a 5-parameter model which achieves a good compromise between simplicity and accuracy, and an alternate 15 parameter model achieves better accuracy with some loss of simplicity.

I. INTRODUCTION

The electronic structure of graphene features π-orbital bands close to the Fermi energy and σ-orbital bands associated with its honeycomb lattice sp$_2$ bonding network.[1] The π and π^* bands that are responsible for most observable electronic properties of graphene are usually described using tight-binding models obtained by fitting either to experiment or to theoretical first principles bands.[1–4] Many qualitative features are correctly captured when only near-neighbor hopping is retained, although more accuracy can be achieved by increasing the number of parameters. For instance, the model introduced many years ago by Wallace[2] includes first and second neighbor hopping terms. Another useful model retains only nearest neighbor hopping, but introduces an additional parameter to allow for a finite overlap between orbitals[1] localized on neighboring sites. Both improvements make it possible to account for the electron-hole asymmetry of graphene's band structure. More recent work[3] based on the SIESTA[5] *ab initio* simulation software has provided a model which includes up to the third nearest neighbor hopping terms with finite overlaps between neighboring localized orbitals and provides a better fit of the bands over a broader energy range. An alternate and physically more transparent hopping tight-binding model has been obtained using a similar scheme.[4] More accurate tight-binding models are sometimes important in understanding the electronic properties of grapheme sheets, for example in deciding whether deviations from the near-neighbor model should be ascribed to band or many-body effects.

In this paper we explore graphene tight-binding models from the point of view of maximally localized Wannier[6] functions. The Wannier approach provides a physically intuitive but fully rigorous representation of graphene's π-bands.[7] In the Wannier representation the band Hamiltonian is succinctly represented in terms of parameters with an intuitive physical meaning as amplitudes for electron hopping from one site to another; the more physically opaque overlap parameters of some LCAO theories vanish exactly because of the orthonormality of the Wannier basis set. There is however a gauge freedom[8] in Wannier function construction that can mod-

ify localization details and hopping parameters. One useful and physically meaningful prescription is to construct maximally localized Wannier functions which minimize spread relative to localization centers.[6] The numerical calculations we present are based on the maximally localized Wannier function method implemented in the software package *wannier90*[9] which postprocesses Bloch wave functions obtained from first principles calculations.

Our aim is to provide a tight-binding model for graphene that accurately reproduces the first principles local density approximation[10] bands produced by plane-wave psedopotential calculations as implemented in Quantum Espresso.[11] The numerical values of the hopping parameters thus obtained provide a highly accurate tight-binding fit to the *ab initio* π, π^* bands throughout the Brillouin zone. We explicitly discuss the role played by remote neighbor hopping terms in these models, explaining how they are related to the Fermi velocity value, and to the trigonal warping and particle-hole symmetry breaking. Our paper is structured as follows. In section II we briefly summarize some of the ideas behind the Wannier function basis construction implemented in *wannier90*, and explain some details of this particular application of the maximally-localized Wannier method. In section III we present several tight-binding model approximations to the graphene π-bands model, some including up to seventeen distinct hopping parameter. We close the paper with a conclusions and discussion section, in which we focus on the merits of the recommended models.

II. MAXIMALLY LOCALIZED WANNIER FUNCTIONS IN GRAPHENE FROM DFT CALCULATIONS

Bloch states in topologically trivial solids can always be expanded in terms of localized Wannier orbitals. Because of the arbitrary k-dependent Bloch-state phase, Wannier functions are not unique. Our study is based on the *wannier90* tool developed by Marzari and collaborators[9] which constructs maximally localized Wannier functions (MLWF) that minimize the spread of density probability around localization centers. We performed initial band-structure calculations using the quantum espresso code[11] with the ultrasoft C.pz-rrkjus
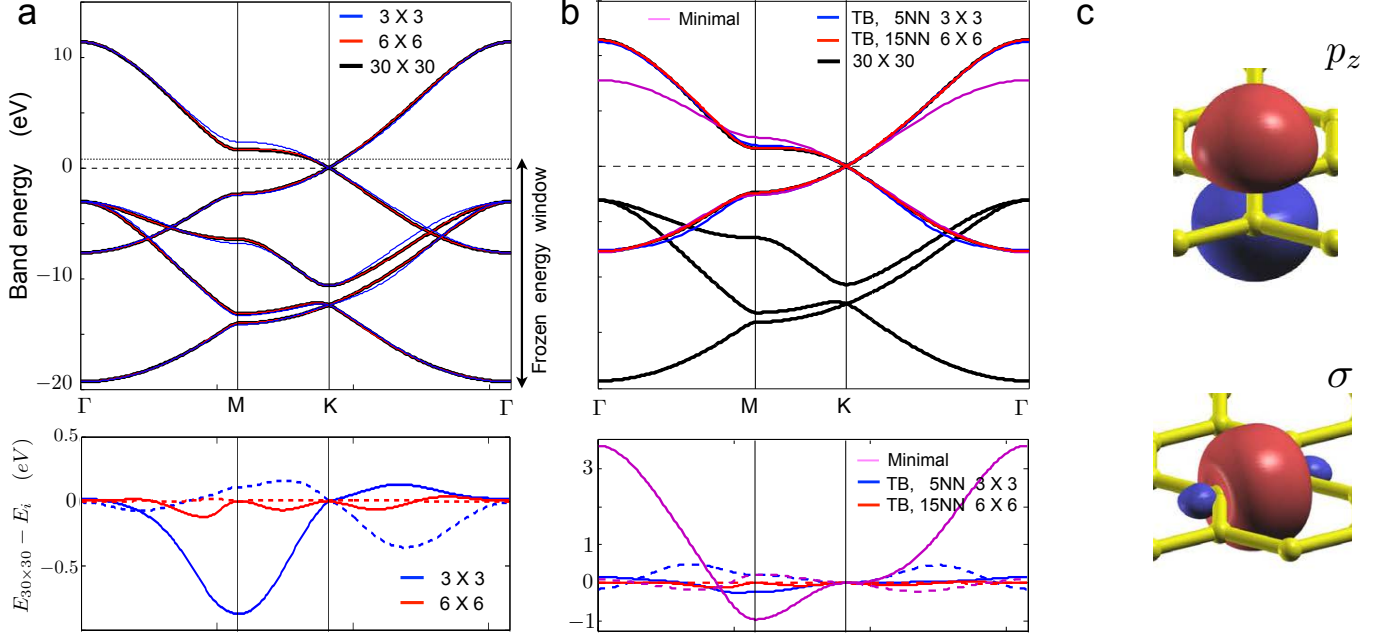
FIG. 1: (Color online) **a**. Band structure of graphene obtained through Wannier interpolation of first principles LDA results for three different k-point sampling densities. The potential was constructed from a common converged charge density obtained using a 36×36 mesh. Differences between the coarser sampling bands and the reference 30×30 sampling bands are shown below using solid (dashed) lines for the π-conduction (valence) bands. Note that the conduction band energy near the Brillouin-zone edge M point is most sensitive to the Wannier interpolation. **b**. Tight-binding band structures for different hopping parameter sets. The bands of the commonly used minimal model (pink) that has nearest neighbor hopping only is also shown for comparison. The minimal model hopping parameter chosen was $t_1 = -2.59$ eV to match the Dirac point velocity of the *ab initio* bands. The black solid lines plot the same reference bands as in the left panel, whereas the blue and red lines represent the tight-binding model bands obtained from 3×3 sampling which results in 5 independent hopping parameters (see Tables I, IV), and the 15-band model implied by by 6×6 sampling. Note that the 5 nearest neighbor tight-binding model gives more accurate band structures than the 3×3 interpolated bands with a maximum error of about 2% of the bandwidth, whereas the 15 neighbor model is essentially identical to the 6×6 interpolated bands. The five parameter model follows the *ab-initio* bands reasonably accurately over the full Brillouin zone using a small number of parameters. The panel below plots differences relative to the reference bands. **c**. Surface plots for the maximally localized π-band and σ bonding orbital Wannier functions. The red and blue regions indicate positive and negative values of the real part of the wave function amplitudes. Adapted from Ref. [8].

pseudopotential which is based on the Perdew-Zunger[12] local-density-approximation (LDA)[10] exchange-correlation potential parameterization. We used a kinetic-energy cutoff of 80 Ry for the plane-wave expansion and calculated the self-consistent ground state using a $36 \times 36 \times 1$ Monkhorst-Pack mesh of k-points and a Fermi distribution edge fictitiously smeared by 0.02 Ry. Starting from a self-consistent charge density obtained in this way we evaluated up to 36 bands on different sets of $n_{k_x} \times n_{k_y} \times 1$ k-point grids. The required input overlap matrices and projections were calculated using the post-processing routine *pw2wannier90* supplied with quantum espresso. For the maximally localized Wannier function calculation we used atom centered projections of the p_z orbitals for the π, π^*-bands of graphene and bond centered s orbitals for the bonding σ bands as initial guesses, and then ran *wannier90* to obtain optimized MLWFs, following procedures similar to those explained in Refs. [8,9]. We fixed the upper limit of the frozen energy window to be 1 eV above the Dirac point for the disentanglement procedure and set the maximum number of iterative steps to 300, which proved to

be more than sufficient to converge the MLWFs and works particularly well for graphene. The Wannier function spread for the p_z orbitals are discussed in appendix A and their numerical values gathered in Table III.

One advantage of the Wannier interpolation method is the possibility in some systems of accurately parameterizing first principles band structures across the entire Brillouin zone with a small number of parameters that can be extracted from a coarse k-point sampling.[13] In the case of graphene a rather limited $6 \times 6 \times 1$ k-point sampling density with two atoms in the unit cell already leads to Wannier interpolated bands that are practically indistinguishable from the fully converged *ab initio* bands obtained from interpolation of a 30×30 k-points sampling calculation as shown in Fig. 1. Some discrepancies are visible to the naked eye when we use a lower sampling density of $3 \times 3 \times 1$. The density of k-point sampling defines the system size beyond which all properties are periodic, and therefore limits the maximum number of physically meaningful nearest neighbor hopping terms that can be used to reproduce the bands in the system. For a $3 \times 3 \times 1$ sampling density
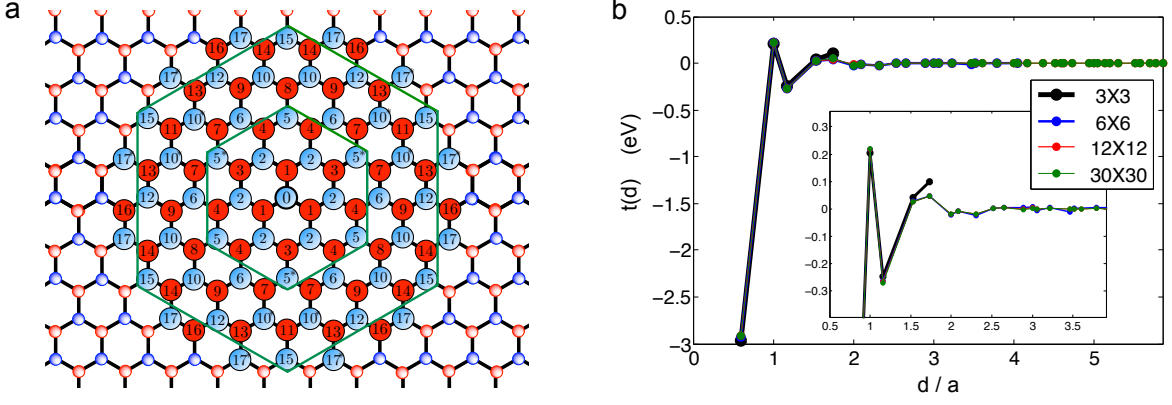
FIG. 2: (Color online) **a.** Honeycomb lattice neighbors m as defined in Tables V and VI grouped by symmetry. The central site (0) in this illustration is on the A (blue) sublattice and the three 1st near neighbors are on the B (red) sublattice. The inner and outer hexagons indicate the hopping processes included in 5 and 15 neighbor tight-binding models. **b.** Hopping amplitude $t(d)$ as a function of the real space distance d between the carbon lattice sites for Wannier models implied by different **k**-point sampling densities. The inset highlights differences between remote hopping amplitudes.

only 5 nearest neighbor hopping terms are properly defined (see Table I).

III. π-BAND TIGHT-BINDING HAMILTONIANS

Because there is one π-electron per site, the π-band tight-binding Hamiltonian is a 2×2 matrix:

$$H(\mathbf{k}) \;=\; \begin{pmatrix} H_{AA}(\mathbf{k}) & H_{AB}(\mathbf{k}) \\ H_{BA}(\mathbf{k}) & H_{BB}(\mathbf{k}) \end{pmatrix}. \tag{1}$$

The Bloch function basis function for this Hamiltonian is related to the Wannier functions by

$$|\psi_{\mathbf{k}\alpha}\rangle \;=\; \frac{1}{\sqrt{N}} \sum_{\mathbf{R}} e^{i\mathbf{k}(R+\tau_{\alpha})} |\mathbf{R} + \tau_{\alpha}\rangle \tag{2}$$

where α is the sublattice index, τ_{α} is the position of the sublattice relative to the lattice vectors $\mathbf{R}$ and $|\mathbf{R} + \tau_{\alpha}\rangle$ is a Wannier function. The matrix elements of the Hamiltonian are related to the Wannier representation hopping amplitudes by

$$H_{\alpha\beta}(\mathbf{k}) \;=\; \langle \psi_{\mathbf{k}\alpha} | H | \psi_{\mathbf{k}\beta} \rangle \tag{3}$$

$$=\; \frac{1}{N} \sum_{\mathbf{RR'}} e^{i\mathbf{k}(\mathbf{R'}-\mathbf{R})} t_{\alpha\beta}(\mathbf{R} - \mathbf{R'}) \tag{4}$$

where

$$t_{\alpha\beta}(\mathbf{R} - \mathbf{R'}) \;=\; \left\langle \mathbf{R} + \tau_{\alpha} \,|\, H \,|\, \mathbf{R'} + \tau'_{\beta} \right\rangle \tag{5}$$

represents tunneling from β to α sublattice sites located respectively at $\mathbf{R'} + \tau'_{\beta}$ and $\mathbf{R} + \tau_{\alpha}$. It follows from inversion symmetry that $H_{AA}(\mathbf{k}) = H_{BB}(\mathbf{k})$.

By grouping neighbor vectors related by symmetry, the Hamiltonian matrix elements can be expressed as a sum over

neighbor indices n:

$$H_{AB}(\mathbf{k}) = \sum_n t_n \, f_n(\mathbf{k}) \tag{6}$$

or

$$H_{AA}(\mathbf{k}) = \sum_n t'_n g_n(\mathbf{k}) \tag{7}$$

where $t_n = t_{ABn}$ and $t'_n = t'_{AAn}$ are the common hopping of members of the set of nth neighbors for a given sublattice and $f_n(\mathbf{k})$ and g_n are the corresponding structure factors obtained by summing phase factors $\exp(i\vec{k} \cdot \vec{R})$ over this set.[14] Additional discussions on the role of distant hopping terms can be found in appendix B. It is useful to distinguish neighbor groups that are off-diagonal in sublattice from those that are diagonal. The positions of the distant neighbors from a reference site 0 at the origin are shown in Fig. 2 where we use the blue and red colors to distinguish A and B sublattices. We have chosen a coordinate system in which the honeycomb's Bravais lattice has primitive vectors

$$\vec{a}_1 = a(1,0)\,, \qquad \vec{a}_2 = a\left(\frac{1}{2}, \frac{\sqrt{3}}{2}\right), \tag{8}$$

where $a = 2.46$Å is the lattice constant of graphene. The self-consistent LDA lattice constant we obtained was $a = 2.44$, about 1% smaller, and yields a converged nearest neighbor hopping of $t = -2.99$, see Table IV in appendix C, a value about 2-3 % greater than the results quoted in table I. The reciprocal lattice vectors are then

$$\vec{b}_1 = \frac{4\pi}{\sqrt{3}a}\left(\frac{\sqrt{3}}{2}, -\frac{1}{2}\right)\,, \quad \vec{b}_2 = \frac{4\pi}{\sqrt{3}a}(0,1). \tag{9}$$

We choose $\tau_{\alpha} = (0,0)$ and $\tau_{\beta} = (0, a/\sqrt{3})$. Numerical values of the inter-lattice hopping parameters implied by different k-space sampling densities are plotted in Fig. 4 and
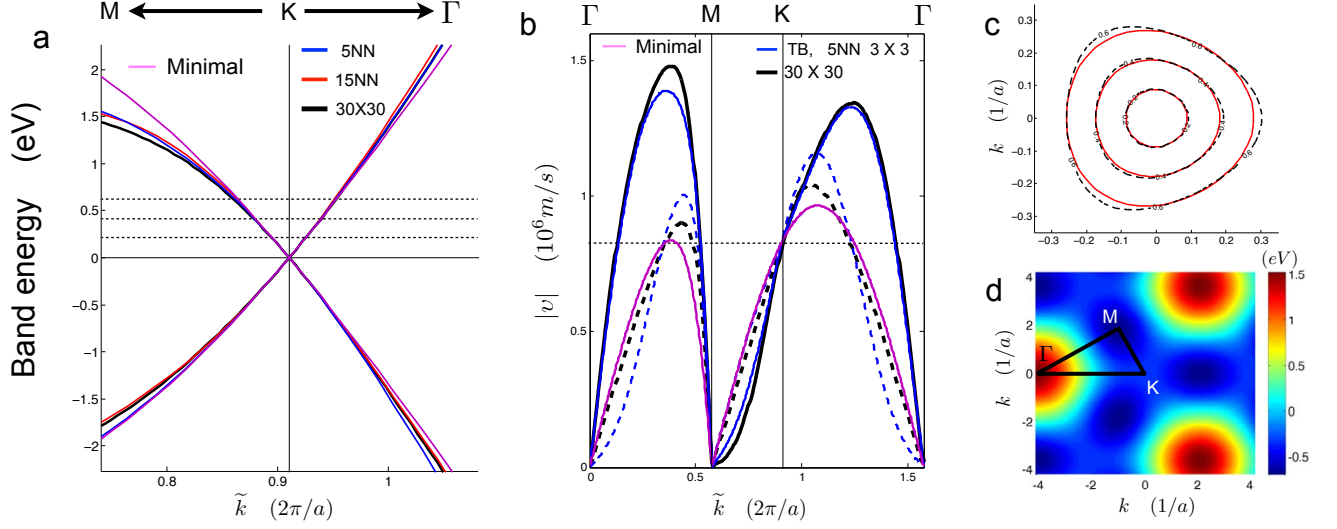
FIG. 3: (Color online) **a**. Band structure estimates near the Dirac point obtained using the minimal model, using the five hopping parameter model extracted from the from 3×3 calculation, and using the 15 hopping parameter model extracted from 6×6 k-point sampling, compared to the interpolated reference bands in solid black lines. The dotted horizontal lines show the energy cuts used for the contour plots in **c**. **b**. Absolute value of quasiparticle velocities $\upsilon = \partial E / \hbar \partial k$ for the minimal model, the five nearest neighbor model, and the reference *ab initio* bands. The dotted horizontal line at $\upsilon = 0.838 \cdot 10^6$ m/s specify the Fermi velocity at the Dirac point. The solid lines represent conduction bands quasiparticle velocities and the dashed lines correspond to valence band velocities. Note that the velocity vanishes in both conduction and valence bands at the $\vec{k} = M$ van Hove singularity point. **c**. Contour lines of the energy bands in **a**. for the minimal and reference band model for 0.2, 0.4 and 0.6 eV. **d**. Color scale plot of $H_{AA}(\mathbf{k})$ calculated using 17 nearest neighbor hopping terms. The combined effect of second and fifth nearest neighbor hopping terms is able to account for the negative inverted parabolic correction near K, the more pronounced negative corrections near M and large positive corrections near Γ.

listed in tables V and I. The translation vectors for each group of neighbors, the associated structure factors, and their expansions near the band-crossing Brillouin-zone corner points $\mathbf{k}_D = (4\pi/3a, 0)$ are listed in Tables V, VI.

Because of the inversion symmetry property $H_{AA}(\mathbf{k}) = H_{BB}(\mathbf{k})$, the π-band energies of graphene are given by

$$E_{\pm}(\mathbf{k}) = |H_{AA}(\mathbf{k})| \pm |H_{AB}(\mathbf{k})|. \quad (10)$$

It follows that the velocity at the Dirac point is determined by $|H_{AB}(\mathbf{k})|$, *i.e.* by the inter-sublattice hopping contribution to the Hamiltonian, and that particle-hole symmetry is broken whenever $|H_{AA}(\mathbf{k})| \neq 0$, *i.e.* whenever there is an intra-sublattice contribution. As summarized in Table V, for all inter-sublattice hopping processes $f_n(\mathbf{k})$ vanishes at the Brillouin-zone corner $\mathbf{k}_D = (4\pi/3a, 0)$ and has a leading correction proportional to $q \exp(-i\theta_{\vec{q}})$. Here $\vec{q}$ is wave vector measured from the Brillouin-zone corner. The intra-sublattice processes on the other hand have no linear in q terms and are isotropic to second order in q. The sub-leading term in the expansion of the inter-sublattice terms behaves like $q^2 \exp(2i\theta_{\vec{q}})$.

The low energy $\vec{k} \cdot \vec{p}$ model implied by a given tight-binding parameterization is obtained by performing a Taylor expansion of the bands near the Dirac point K. Intra-sublattice processes contribute to the diagonal elements of the $\vec{k} \cdot \vec{p}$ Hamiltonian whereas inter-sublattice processes contribute to the off-diagonal matrix elements. For the off-diagonal elements for which the Dirac velocity and trigonal warping are specified at

low energies we have

$$H_{\alpha\beta}(\mathbf{k}_D + \mathbf{k}) \simeq C_{\alpha\beta 1} k e^{-i\theta_{\mathbf{k}}} + C_{\alpha\beta 2} k^2 e^{i2\theta_{\mathbf{k}}}, \quad (11)$$

involving sums of f_n terms for matrix elements connecting sites $\alpha\beta = AB$. The explicit form of the expansion coefficients are given by

$$C_{\alpha\beta 1} = \frac{\sqrt{3}a}{2}(-t_1 + 2t_2 + t_3 - 5t_4 - 4t_5 + 7t_6 + 5t_7$$
$$+ 2t_8 - 4t_9 + 11t_{10}) \quad (12)$$

$$C_{\alpha\beta 2} = \frac{a^2}{8}(t_1 + 4t_2 - 13t_3 - t_4 + 16t_5 + 11t_6 + 25t_7$$
$$- 52t_8 - 46t_9 + 47t_{10}). \quad (13)$$

where we have abbreviated the notation by denoting $t_n = t_{\alpha\beta n}$ removing the $\alpha\beta$ subscripts.

For the diagonal elements responsible for particle-hole symmetry breaking as summarized in Table VI we have

$$H_{\alpha\beta}(\mathbf{k}_D + \mathbf{k}) \simeq C'_{\alpha\beta 0} + C'_{\alpha\beta 2} k^2 \quad (14)$$

and their form is given by

$$C'_{\alpha\beta 0} = -3t'_1 + 6t'_2 - 3t'_3 - 6t'_4 + 6t'_5$$
$$+ 6t'_6 - 6t'_7 \quad (15)$$

$$C'_{\alpha\beta 2} = \frac{3a^2}{4}(t'_1 - 6t'_2 + 4t'_3 + 14t'_4$$
$$- 18t'_5 - 6t'_6 + 26t'_7). \quad (16)$$

AB	n	m	N^0	d_n/a	$t_{n,3\times3}$	$t_{n,6\times6}$	$t_{n,12\times12}$	$t_{n,30\times30}$
1	1	3	$\frac{1}{\sqrt{3}}$	-3.00236	-2.94015	-2.92774	-2.92181
2	3	3	$\frac{2}{\sqrt{3}}$	-0.22464	-0.26199	-0.27586	-0.27897
3	4	6	$\sqrt{\frac{7}{3}}$	0.05205	0.03172	0.02807	0.02669
4	7	6	$\sqrt{\frac{13}{3}}$		-0.00830	-0.00727	-0.00885
5	8	3	$\frac{4}{\sqrt{3}}$		-0.02463	-0.01812	-0.01772
6	9	6	$\sqrt{\frac{19}{3}}$		0.00096	0.00463	0.00675
7	11	3	$\frac{5}{\sqrt{3}}$		0.00467	-0.00227	-0.00262
8	13	6	$\sqrt{\frac{28}{3}}$		-0.00724	-0.00088	0.00019
9	14	6	$\sqrt{\frac{31}{3}}$		0.00562	0.00044	-0.00068
10	16	6	$\sqrt{\frac{37}{3}}$			-0.00230	-0.00237

AA	n	m	N^0	d_n/a	$t'_{n,3\times3}$	$t'_{n,6\times6}$	$t'_{n,12\times12}$	$t'_{n,30\times30}$
1	2	6	1	0.20509	0.21813	0.22377	0.22378
2	5	6	$\sqrt{3}$	0.06912	0.04357	0.04555	0.04813
3	6	6	2		-0.02379	-0.02406	-0.02402
4	10	12	$\sqrt{7}$		0.00538	0.00313	0.00263
5	12	6	3		0.00783	0.00296	0.00111
6	15	6	$\frac{6}{\sqrt{3}}$		-0.01429	-0.00110	0.00018
7	17	12	$\sqrt{\frac{39}{3}}$			-0.00066	-0.00008

TABLE I: Hopping amplitudes in eV units implied by four different **k**-point sampling densities. Intra-sublattice and inter-sublattice amplitudes are grouped separately. The two models on the left, with five and fifteen parameters respectively, provide good compromises between accuracy and simplicity.

	exp. $a = 2.46 \mathring{A}$		LDA $a = 2.439 \mathring{A}$	
	5 n.n.	15 n.n.	5 n.n.	15 n.n.
C'_{AA2} (eV·$\mathring{A}^2$)	-0.951	-0.537	-1.01	-0.572
C_{AB1} (eV·$\mathring{A}$)	5.55	5.50	5.62	5.57
C_{AB2} (eV·$\mathring{A}^2$)	-3.46	-3.44	-3.50	-3.48

TABLE II: Expansion coefficients for the effective two-dimensional continuum model Hamiltonian near the Dirac point $\mathbf{k}_D = (4\pi/3a, 0)$. The C_{AB1} term is related with the Fermi velocity through $v_F = C_{AB1}/\hbar$. Both the 5 and 15 parameter models give a satisfactory agreement in the main parameters that define the effective continuum model. Although the particle-hole symmetry breaking term given by C'_{AA2} shows the largest discrepancy between both models they have a relatively small effect due to their small values compared to the other two terms. The results between the experimental and self-consistent LDA lattice constant that are different by less than 1% introduce marginal changes in the obtained parameters.

IV. CONCLUSIONS AND DISCUSSIONS

We have discussed graphene π-band tight-binding models derived from maximally localized Wannier functions, assessing the degree to which they reproduce the Dirac velocity, trigonal warping, and particle-hole-symmetry breaking parameters that appear in continuum models of graphene, and their overall accuracy within an eV of the Dirac point. We find that a relatively convenient five near-neighbor tight binding model with three inter-sublattice and two intra-sublattice hopping parameters obtained from a rather coarse 3×3 k-point momentum-space sampling already provides a substantial improvement relative to the commonly used minimal model with only near-neighbor hopping. Accuracy is further improved near the conduction band van Hove singularity by using a fifteen parameter model which retains nine intra-sublattice hopping processes and six inter-sublattice hopping processes. These two models are superior in both accuracy and in the transparency of their physical interpretation compared to previously proposed refinements of the minimal model.

Intra-sublattice particle-hole symmetry breaking effects are most prominent near symmetry points with peaks at Γ and valleys around M and K. These effects require at least up to fifth nearest neighbor hopping terms for a qualitatively correct description. The fifteen parameter model based on 6×6 sampling provides an essentially exact reproduction of the *ab initio* LDA bands.

The models presented here provide a tight-binding platform for graphene electronic property studies which have *ab initio* accuracy. The improved accuracy relative to the minimal model is valuable, especially for applications in which high-energy features of the bands must be accurately captured. Examples that come to mind include optical absorption in visible and near-infrared regimes[15] and putative superconductivity[16–18] in systems with Fermi energies at the van Hove singularities.

Of course, the tight-binding model is only as accurate as the *ab initio* LDA calculation that it approximates. Our use of

for matrix elements connecting the sites $\alpha\beta = AA, BB$ for intra-sublattice hopping parameters involving sums of g_n terms. We have used the primes, both for the expansion coefficients as well as the hopping terms, to remark they involve expansions of g_n terms rather than f_n. More distant hopping processes make a relatively smaller contribution to C_{AA2} as expected. Thus, the continuum model Hamiltonian near $\mathbf{k}_D = (4\pi/3a, 0)$ in terms of the effective parameters can be written as

$$
\begin{aligned}
H^{cont}_{\mathbf{k}_D}(\mathbf{k}) = {} & k^2 C'_{AA2}\mathbb{I} + k C_{AB1} \left(\cos\left(\theta_\mathbf{k}\right)\sigma_x + \sin\left(\theta_\mathbf{k}\right)\sigma_y\right) \\
& + k^2 C_{AB2} \left(\cos\left(2\theta_\mathbf{k}\right)\sigma_x - \sin\left(2\theta_\mathbf{k}\right)\sigma_y\right)
\end{aligned} \tag{17}
$$

where σ_x and σ_y are Pauli matrices. The values of the parameters for expansion near the Dirac point are given in table II, both for the experimental lattice constant and a slightly smaller self-consistent LDA value.

The values of the $\vec{k} \cdot \vec{p}$ parameters corresponding to different tight-binding models are summarized in Fig. 4. We see there that, in addition to providing a good characterization of the overall shape of the bands, the 5 neighbor tight-binding model accurately characterizes the three most important continuum model band parameters. The main advantage of the 15 parameter model is that it provides a more accurate description of the conduction band van Hove singularity.
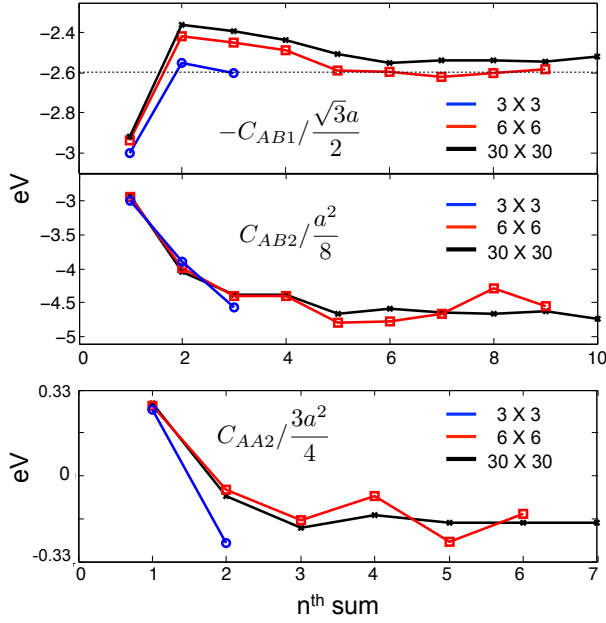
FIG. 4: (Color online) Leading low-energy graphene continuum model band parameters implied by different Wannier interpolations. For the three models considered these plots show the dependence on hopping-parameter truncation at different neighbor shells. C_{AB1}, C_{AB2}, and C_{AA2} are respectively the velocity, trigonal warping, and particle-hole symmetry breaking parameters for continuum $\vec{k} \cdot \vec{p}$ models and are defined in Eqs. (12-13) and (15-16). The dashed horizontal line in the C_{AB1} plot is the minimal model tight-binding model fit to the *ab-initio* LDA band structure Dirac point velocity. The five neighbor model obtained from 3×3 k-point sampling Wannier interpolation produces accurate values of the coefficients for the Fermi velocity and parabolic off diagonal correction.

the LDA approximation is intentional since we wish to construct bands that have a realistic bonding structure, but want as far as possible to construct a model which does not already reflect the peculiar π-band[19–21] exchange and correlation effects which increase Fermi velocities in low-carrier density systems when disorder is weak and reshape[22] Dirac cones. It is well known, for example, that many-body physics is necessary in particular to explain the divergence of the Fermi level quasiparticle velocity at vanishing carrier density[22], photoelmission satellites[23] and the plasmaron features near the Dirac point in ARPES spectra when the carrier density is finite.[24] Many-body effects must be accounted for separately because their influence depends on the observable under study, in addition to being dependent on carrier-density and disorder. For many low-energy phenomena, the influence of interactions can often be accounted for simply by renormalizing the Fermi velocity, or equivalently by renormalizing hopping parameters. Many body velocity enhancements are likely responsible for the fact that near-neighbor hopping parameters that are obtained by fitting to experimental data are normally larger than those of our tight-binding models.

The present analysis suggests that the minimal near-neighbor tight-binding model often used for graphene pro-

vides an adequate description of many properties not because hopping really is very short-ranged, and instead because the low-energy bands depend only on the Dirac-point velocity. Presumably the same is true of inter-layer hopping terms. The range of inter-layer hopping processes plays a key role in assessing the influence of relative layer alignment[25–28] on the electronic structure of graphene on graphene and graphene on boron nitride. The maximally-localized Wannier approach should prove equally valuable for those closely related electronic structure problems.

Appendix A: Wannier Function Spread

Wannier functions constructed from an *ab initio* calculation with a finite density of k-points have a density which is localized near points separated by a distance inversely related to the coarseness of the k-point mesh. The spread of the Wannier wave functions around their centers provides estimates of atomic orbital size. A mean-square characteristic is defined by[8]

$$\Omega = \sum_n \langle (\mathbf{r} - \bar{\mathbf{r}}_n)^2 \rangle = \Omega_I + \widetilde{\Omega}, \qquad (A1)$$

where n is the index of each Wannier function and $\bar{\mathbf{r}}_n$ its center. Here Ω_I is a gauge invariant contribution to the spreading that remains fixed for a given choice of band subspace, whereas $\widetilde{\Omega}$ can be minimized through iterative unitary transformations as explained in reference [9]. The dependence of orbital spreading on k-point sampling density is weak in the case of graphene, as we show in Table III, which hints that a relatively coarse sampling of the k-points produces a physically realistic model. The slow increase of the Wannier-function spread with k-point mesh density may reflect the strong dependence of interlayer-sublattice phase on momentum near the band-crossing Dirac point.[21]

	3×3	6×6	12×12	30×30
Ω_{p_z}	0.8237	0.9168	0.9571	0.9750
Ω_σ	0.5223	0.5875	0.6074	0.6134
Ω_{total}	3.2143	3.5960	3.7365	3.7900
Ω_I	2.4951	2.8437	2.9844	3.0380

TABLE III: Evolution of wave function spread with k-point sampling density given in $\mathring{A}^2$. We attribute the increase in spread with k-point density to the strong dependence of wave function on momentum near the Dirac point.

Appendix B: Role of distant neighbor hopping terms

The role played by remote neighbors in modifying the band dispersion is best illustrated by comparing with the minimal nearest neighbor model bands, plotted in Fig. 1 and magnified near the Dirac point in Fig. 3. The inter-sublattice hopping terms are responsible for the main features in the band dispersion, including the trigonal distortions near the Dirac point. The nearest neighbor amplitude has the largest value and already captures the bands qualitatively. As we can see in Table II the third neighbor hopping process is responsible for a substantial reduction in the trigonal distortion produced by first neighbor hopping. In Fig. 4 we plot equal magnitude contours for individual remote neighbor contributions. The more remote neighbors play a less essential role because of hopping amplitude decreases. The strength of trigonal warping is reflected by the difference in band dispersion around the Dirac cone between the $\Gamma - K$ and $K - M$ directions, as illustrated in Fig. 3.
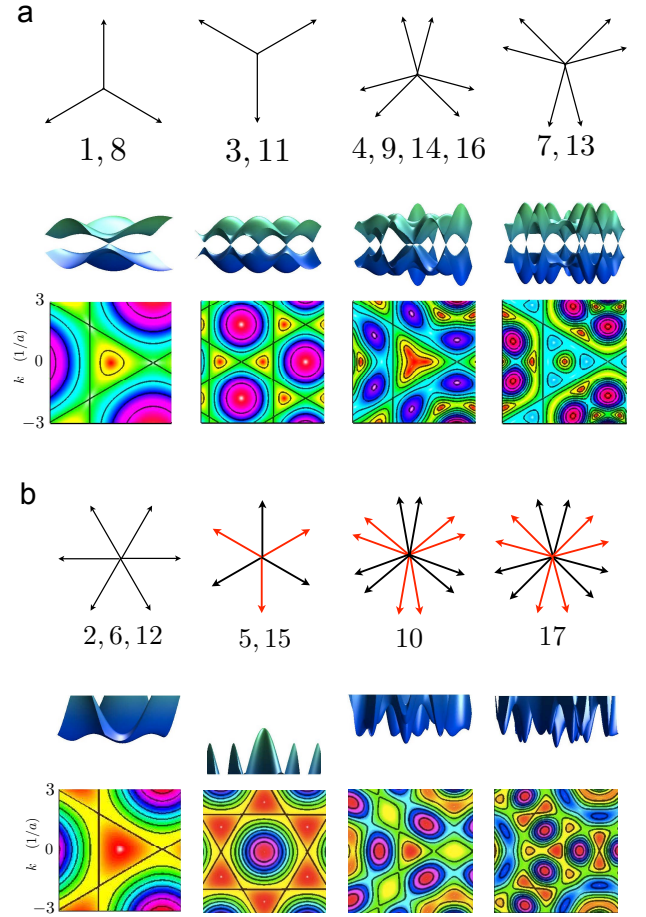

FIG. 5: **a.** Individual neighbor shell contributions to the band Hamiltonian. The role of inter-sublattice hopping terms is illustrated using conduction band surface and contour-plots for the bands obtained for neighbor sheels 1, 3, 4, and 7 with the hopping parameter set to $t_{nAB} = 1$ eV. More distant neighbors give features that vary more rapidly in momentum space. **b.** Similar plots for intra-sublattice contributions from neighbor shells 2,5,10, and 17. We have indicated with red arrows those sites labeled with an asterisk in Table VI.

The intra-sublattice hopping terms that account for the particle-hole symmetry breaking are examined in Fig. 3b. There are at least six hopping sites for a given n^{th}-distant neighbor hopping whose contributions to the bands are illustrated in Fig. 4. From an inspection of Figs. 3d, 4 and the hopping terms gathered in Tables I, IV we can observe that the 2nd distant hopping term alone captures correctly the positive correction to the bands near the Γ, but fails to capture features near M and K points. The 5th neighbor hopping is responsible for dips of the diagonal terms near M and K and also plays an important role in reversing the sign of the leading parabolic particle-hole correction term near K. We conclude that all main features in the bands can be captured by a five neighbor tight-binding model.

Appendix C: Tight-Binding Model at the LDA lattice constant

The results we have reported in the main text were calculated using the experimental lattice constant of $a = 2.46\mathring{A}$ in graphene. The self-consistent LDA lattice constant of $a = 2.439\mathring{A}$, gives rise to a value that is 0.85% smaller and thus the resulting changes are expected to be negligibly small. The new set of hopping parameters are similar to those in Table II and are listed here for sake of completeness

AB	n	m	N^0	d_n/a	$t_{\alpha\beta n,3\times3}$	$t_{\alpha\beta n,6\times6}$	$t_{\alpha\beta n,12\times12}$	$t_{\alpha\beta n,30\times30}$
	1	1	3	$\frac{1}{\sqrt{3}}$	-3.07504	-3.01006	-2.99727	-2.99251
	2	3	3	$\frac{2}{\sqrt{3}}$	-0.23442	-0.27298	-0.28745	-0.28983
	3	4	6	$\sqrt{\frac{7}{3}}$	0.05350	0.03278	0.02903	0.02791
	4	7	6	$\sqrt{\frac{13}{3}}$		-0.00884	-0.00775	-0.00877
	5	8	3	$\frac{4}{\sqrt{3}}$		-0.02594	-0.01925	-0.01870
	6	9	6	$\sqrt{\frac{19}{3}}$		0.00095	0.00490	0.00621
	7	11	3	$\frac{5}{\sqrt{3}}$		0.00485	-0.00252	-0.00256
	8	13	6	$\sqrt{\frac{28}{3}}$		-0.00752	-0.00087	-0.00018
	9	14	6	$\sqrt{\frac{31}{3}}$		0.00591	0.00047	-0.00033
	10	16	6	$\sqrt{\frac{37}{3}}$			-0.00246	-0.00264

AA	n	m	N^0	d_n/a	$t'_{n,3\times3}$	$t'_{n,6\times6}$	$t'_{n,12\times12}$	$t'_{n,30\times30}$
	1	2	6	1	0.21264	0.22614	0.23205	0.23206
	2	5	6	$\sqrt{3}$	0.07326	0.04584	0.04780	0.04969
	3	6	6	2		-0.02478	-0.02518	-0.02499
	4	10	12	$\sqrt{7}$		0.00564	0.00337	0.00285
	5	12	6	3		0.00826	0.00308	0.00204
	6	15	6	$\frac{6}{\sqrt{3}}$		-0.01492	-0.00114	-0.00014
	7	17	12	$\sqrt{\frac{39}{3}}$			-0.00072	-0.00029

TABLE IV: Same as the table I but calculated using a self-consistent lattice constant of $a = 2.439\mathring{A}$ about 1% smaller than the experimental value $a = 2.46\mathring{A}$. gathering the hopping terms between the p_z orbitals as a function of distance for different sampling of **k**-point densities, where we distinguish the inter-sublattice hopping giving rise to the band dispersion and intra-sublattice hopping that accounts for particle-hole symmetry breaking.

n	m	N^0	d_n/a	τ	$f_n(\mathbf{k})$	$f_n^{cont}(\mathbf{k}_D + \mathbf{k})$
1	1	3	$\frac{1}{\sqrt{3}}$	$\tau_1 = (0, \frac{1}{\sqrt{3}})$, $\tau_{2,3} = (\pm\frac{1}{2}, -\frac{1}{2\sqrt{3}})$	$e^{i\frac{k_y a}{\sqrt{3}}} + 2e^{-i\frac{k_y a}{2\sqrt{3}}}\cos(\frac{k_x a}{2})$	$-\frac{\sqrt{3}a}{2}k\,e^{-i\theta_\mathbf{k}} + \frac{a^2}{8}e^{i2\theta_\mathbf{k}}$
2	3	3	$\frac{2}{\sqrt{3}}$	$\tau_{1,2} = (\pm1, \frac{1}{\sqrt{3}})$, $\tau_3 = (0, -\frac{2}{\sqrt{3}})$	$e^{-i\frac{k_y a}{\sqrt{3}}} + 2e^{i\frac{k_y a}{2\sqrt{3}}}\cos(k_x a)$	$\sqrt{3}ak\,e^{-i\theta_\mathbf{k}} + \frac{a^2}{2}e^{i2\theta_\mathbf{k}}$
3	4	6	$\sqrt{\frac{7}{3}}$	$\tau_{1,2} = (\pm\frac{1}{2}, \frac{5}{2\sqrt{3}})$, $\tau_{3,4} = (\pm\frac{3}{2}, -\frac{1}{2\sqrt{3}})$, $\tau_{5,6} = (\pm1, -\frac{2}{\sqrt{3}})$	$2e^{i\frac{k_y 5a}{2\sqrt{3}}}\cos(\frac{k_x a}{2}) + 2e^{-i\frac{k_y a}{2\sqrt{3}}}\cos(\frac{k_x 3a}{2}) + 2e^{-i\frac{k_y 2a}{\sqrt{3}}}\cos(k_x a)$	$\frac{\sqrt{3}a}{2}k\,e^{-i\theta_\mathbf{k}} - \frac{13a^2}{8}e^{i2\theta_\mathbf{k}}$
4	7	6	$\sqrt{\frac{13}{3}}$	$\tau_{1,2} = (\pm2, \frac{1}{\sqrt{3}})$, $\tau_{3,4} = (\pm\frac{3}{2}, \frac{5}{2\sqrt{3}})$, $\tau_{5,6} = (\pm\frac{1}{2}, -\frac{7a}{2\sqrt{3}})$	$e^{i\frac{k_y a}{\sqrt{3}}}\cos(k_x 2a) + 2e^{i\frac{k_y 5a}{2\sqrt{3}}}\cos(\frac{k_x 3a}{2})e^{-i\frac{k_y 2a}{\sqrt{3}}}\cos(\frac{k_x a}{2})$	$-\frac{5\sqrt{3}a}{2}k\,e^{-i\theta_\mathbf{k}} - \frac{a^2}{8}e^{i2\theta_\mathbf{k}}$
5	8	3	$\frac{4}{\sqrt{3}}$	$\tau_1 = (0, \frac{4}{\sqrt{3}})$, $\tau_{2,3} = (\pm2, -\frac{2}{\sqrt{3}})$	$e^{i\frac{k_y 4a}{\sqrt{3}}} + 2\cos(k_x 2a)e^{-i\frac{k_y 2a}{\sqrt{3}}}$	$-2\sqrt{3}ak\,e^{-i\theta_\mathbf{k}} + 2a^2 e^{i2\theta_\mathbf{k}}$
6	9	6	$\sqrt{\frac{19}{3}}$	$\tau_{1,2} = (\pm1, \frac{4}{\sqrt{3}})$, $\tau_{3,4} = (\pm\frac{5}{2}, -\frac{1}{2\sqrt{3}})$	$2e^{i\frac{k_y 4a}{\sqrt{3}}}\cos(k_x a) + 2\cos(\frac{k_x 5a}{2})e^{-i\frac{k_y a}{2\sqrt{3}}} + 2\cos(\frac{k_x 3a}{2})e^{-i\frac{k_y 7a}{2\sqrt{3}}}$	$\frac{7\sqrt{3}a}{2}k\,e^{-i\theta_\mathbf{k}} + \frac{11a^2}{8}e^{i2\theta_\mathbf{k}}$
7	11	3	$\frac{5}{\sqrt{3}}$	$\tau_{1,2} = (\pm\frac{5}{2}, \frac{5}{2\sqrt{3}})$, $\tau_3 = (0, -\frac{5}{\sqrt{3}})$	$2e^{i\frac{k_y 5a}{2\sqrt{3}}}\cos(\frac{k_x 5a}{2}) + e^{-i\frac{k_y 5a}{\sqrt{3}}}$	$\frac{5\sqrt{3}a}{2}k\,e^{-i\theta_\mathbf{k}} + \frac{25a^2}{8}e^{i2\theta_\mathbf{k}}$
8	13	6	$\sqrt{\frac{28}{3}}$	$\tau_{1,2} = (\pm2, \frac{4}{\sqrt{3}})$, $\tau_{3,4} = (\pm3, \frac{1}{\sqrt{3}})$, $\tau_{5,6} = (\pm1, -\frac{5}{\sqrt{3}})$	$2\cos(k_x 2a)e^{i\frac{k_y 4a}{\sqrt{3}}} + 2\cos(k_x 3a)e^{i\frac{k_y 2a}{\sqrt{3}}} + 2\cos(k_x a)e^{-i\frac{k_y 5a}{\sqrt{3}}}$	$-\sqrt{3}ak\,e^{-i\theta_\mathbf{k}} - \frac{13a^2}{2}e^{i2\theta_\mathbf{k}}$
9	14	6	$\sqrt{\frac{31}{3}}$	$\tau_{1,2} = (\pm\frac{1}{2}, \frac{11}{2\sqrt{3}})$, $\tau_{3,4} = (\pm3, -\frac{2}{\sqrt{3}})$, $\tau_{5,6} = (\pm\frac{5}{2}, -\frac{7}{2\sqrt{3}})$	$2\cos(\frac{k_x a}{2})e^{i\frac{k_y 11a}{2\sqrt{3}}} + 2\cos(k_x 3a)e^{-i\frac{k_y 2a}{\sqrt{3}}} + 2\cos(\frac{k_x 5a}{2})e^{-i\frac{k_y 7a}{2\sqrt{3}}}$	$2\sqrt{3}ae^{-i\theta_\mathbf{k}} - \frac{23a^2}{4}e^{i2\theta_\mathbf{k}}$
10	16	6	$\sqrt{\frac{37}{3}}$	$\tau_{1,2} = (\pm\frac{7}{2}, -\frac{1}{2\sqrt{3}})$, $\tau_{3,4} = a(\pm\frac{5}{2}, \frac{11}{2\sqrt{3}})$, $\tau_{5,6} = (\pm2, -\frac{5}{\sqrt{3}})$	$2\cos(\frac{k_x 7a}{2})e^{-i\frac{k_y a}{2\sqrt{3}}} + 2\cos(\frac{k_x 5a}{2})e^{i\frac{k_y 11a}{2\sqrt{3}}} + 2\cos(k_x 2a)e^{-i\frac{k_y 5a}{\sqrt{3}}}$	$-\frac{11\sqrt{3}a}{2}k\,e^{-i\theta_\mathbf{k}} + \frac{47a^2}{8}e^{i2\theta_\mathbf{k}}$

TABLE V: Summary of the distant neighbor contributions in the Hamiltonian matrix elements for inter-sublattice terms. The letter n denotes the index for the nearest neighbor sites for a given sublattice, m is the distant neighbor index when both sublattices are considered and correspond to the numbers as labeled in Fig. 1. N^0 is the number of lattice sites contributing in the structure factor consisting of nth nearest neighbor terms, $f_n(\mathbf{k})$ is the analytic expression of the structure factor corresponding to the nth neighbor contribution to the Hamiltonian matrix element and $f_n^{cont}(\mathbf{k}_D + \mathbf{k})$ is the continuum approximation near the Dirac point of the aforementioned Hamiltonian matrix element term.

n	m	N^0	d_n/a	τ	$g_n(\mathbf{k})$	$g_n^{cont}(\mathbf{k}_D + \mathbf{k})$
0	0	1	0	$\tau_1 = (0,0)$	1	1
1	2	6	1	$\tau_{1,2} = (\pm1, 0)$, $\tau_{3,4} = (\pm\frac{1}{2}, \frac{\sqrt{3}}{2})$, $\tau_{5,6} = (\pm\frac{1}{2}, -\frac{\sqrt{3}}{2})$	$2\cos(k_x a) + 4\cos(\frac{k_y \sqrt{3}a}{2})\cos(\frac{k_x a}{2})$	$-3 + \frac{3a^2}{4}k^2$
2	5	3	$\sqrt{3}$	$\tau_1 = (0, \sqrt{3})$, $\tau_{2,3} = (\pm\frac{3}{2}, -\frac{\sqrt{3}}{2})$	$e^{ik_y\sqrt{3}a} + 2e^{-i\frac{k_y\sqrt{3}a}{2}}\cos(\frac{k_x 3a}{2})$	$3 - \frac{9a^2}{4}k^2$
2*	5*	3	$\sqrt{3}$	$\tau_1 = (0, -\sqrt{3})$, $\tau_{2,3} = (\pm\frac{3}{2}, \frac{\sqrt{3}}{2})$	$e^{-ik_y\sqrt{3}a} + 2e^{i\frac{k_y\sqrt{3}a}{2}}\cos(\frac{k_x 3a}{2})$	$3 - \frac{9a^2}{4}k^2$
3	6	6	2	$\tau_{1,2} = (\pm2, 0)$, $\tau_{3,4,5,6} = (\pm1, \pm\sqrt{3})$	$2\cos(k_x 2a) + 4\cos(k_x a)\cos(k_y\sqrt{3}a)$	$-3 + 3a^2 k^2$
4	10	6	$\sqrt{7}$	$\tau_{1,2} = (\pm\frac{1}{2}, \frac{9}{2\sqrt{3}})$, $\tau_{3,4} = (\pm2, -\sqrt{3})$, $\tau_{5,6} = (\pm\frac{5}{2}, \frac{\sqrt{3}}{2})$	$2\cos(k_x 2a)e^{ik_y\sqrt{3}a} + 2\cos(\frac{k_x a}{2})e^{-i\frac{k_y 3\sqrt{3}a}{2}} + \cos(\frac{k_x 5a}{2})e^{i\frac{k_y\sqrt{3}a}{2}}$	$-3 + \frac{21a^2}{4}k^2$
4*	10*	6	$\sqrt{7}$	$\tau_{1,2} = (\pm\frac{1}{2}, -\frac{9}{2\sqrt{3}})$, $\tau_{3,4} = (\pm2, \sqrt{3})$, $\tau_{5,6} = (\pm\frac{5}{2}, \frac{\sqrt{3}}{2})$	$2\cos(k_x 2a)e^{-ik_y\sqrt{3}a} + 2\cos(\frac{k_x a}{2})e^{i\frac{k_y 3\sqrt{3}a}{2}} + \cos(\frac{k_x 5a}{2})e^{i\frac{k_y\sqrt{3}a}{2}}$	$-3 + \frac{21a^2}{4}k^2$
5	12	6	3	$\tau_{1,2} = (\pm3, 0)$, $\tau_{3,4,5,6} = (\pm\frac{3}{2}, \pm\frac{9}{2\sqrt{3}})$	$2\cos(k_x 3a) + 4\cos(\frac{k_x 3a}{2})\cos(k_y 3\sqrt{3}a)$	$6 - \frac{27a^2}{2}k^2$
6	15	3	$\frac{6}{\sqrt{3}}$	$\tau_1 = (0, 2\sqrt{3})$, $\tau_{2,3} = (\pm3, -\sqrt{3})$	$2\cos(k_x 3a)e^{-ik_y\sqrt{3}a} + e^{ik_y 2\sqrt{3}a}$	$3 - 9a^2 k^2$
6*	15*	3	$\frac{6}{\sqrt{3}}$	$\tau_1 = (0, -2\sqrt{3})$, $\tau_{2,3} = (\pm3, \sqrt{3})$	$2\cos(k_x 3a)e^{ik_y\sqrt{3}a} + e^{-ik_y 2\sqrt{3}a}$	$3 - 9a^2 k^2$
7	17	6	$\sqrt{\frac{39}{3}}$	$\tau_{1,2} = (\pm1, 2\sqrt{3})$, $\tau_{3,4} = (\pm\frac{7}{2}, -\frac{\sqrt{3}}{2})$, $\tau_{5,6} = (\pm\frac{5}{2}, -\frac{9}{2\sqrt{3}})$	$2\cos(k_x a)e^{ik_y 2\sqrt{3}a} + 2\cos(\frac{k_x 7a}{2})e^{-i\frac{k_y\sqrt{3}a}{2}} + 2\cos(\frac{k_x 5a}{2})e^{-i\frac{k_y 3\sqrt{3}a}{2}}$	$-3 + \frac{39a^2}{4}k^2$
7*	17*	6	$\sqrt{\frac{39}{3}}$	$\tau_{1,2} = (\pm1, -2\sqrt{3})$, $\tau_{3,4} = (\pm\frac{7}{2}, \frac{\sqrt{3}}{2})$, $\tau_{5,6} = (\pm\frac{5}{2}, \frac{9}{2\sqrt{3}})$	$2\cos(k_x a)e^{-ik_y 2\sqrt{3}a} + 2\cos(\frac{k_x 7a}{2})e^{i\frac{k_y\sqrt{3}a}{2}} + 2\cos(\frac{k_x 5a}{2})e^{i\frac{k_y 3\sqrt{3}a}{2}}$	$-3 + \frac{39a^2}{4}k^2$

TABLE VI: Similar to table V for intra-sublattice hopping terms. The sites with labels $n = 2, 4, 6, 7$ have been separated in two groups to distinguish to different crystal symmetries. The function $g_n(\mathbf{k})$ is the analytic expression of the nth neighbor contribution to the Hamiltonian matrix element and $g_{\alpha\beta n}^{cont}(\mathbf{k}_D + \mathbf{k})$ is its continuum approximation near the Dirac point.

[1] R. Saito, G. Dresselhaus, and M. S. Dresselhaus, Physical Properties of Carbon Nanotubes, (Imperial, London, 1998).

[2] P. R. Wallace, Phys. Rev. **71**, 622 (1947).

[3] S. Reich, J. Maultzsch, and C. Thomsen and P. Ordejón, Phys. Rev. B **66**, 035412 (2002).

[4] R. Kundu, Mod. Phys. Lett. B **25**, 163 (2011).

[5] J. M. Soler, E. Artacho, J. D. Gale, A. García, J. Junquera, P. Ordejón and D. Sánchez-Portal, J. Phys.: Cond. Mat. 142745, (2002).

[6] N. Marzari and D. Vanderbilt, Phys. Rev. B **56**, 12847 (1997).

[7] N. W. Ashcroft and D. Mermin, *Solid State Physics*, (Saunders, 1976).

[8] N. Marzari, A. A. Mostofi, J. R. Yates, I. Souza and D. Vanderbilt, Rev. Mod. Phys. **84**, 1419 (2012).

[9] A. A. Mostofi, J. R. Yates, Y.-S. Lee, I. Souza, D. Vanderbilt, N. Marzari, Computer Physics Communications **178**, 685 (2008).

[10] W. Kohn, Rev. Mod. Phys. **71**, 1253 (1999).

[11] P. Giannozzi, S. Baroni, N. Bonini, M. Calandra, R. Car, C. Cavazzoni, D. Ceresoli, G. L. Chiarotti, M. Cococcioni, I. Dabo, A. Dal Corso, S. Fabris, G. Fratesi, S. de Gironcoli, R. Gebauer, U. Gerstmann, C. Gougoussis, A. Kokalj, M. Lazzeri, L. Martin-Samos, N. Marzari, F. Mauri, R. Mazzarello, S. Paolini, A. Pasquarello, L. Paulatto, C. Sbraccia, S. Scandolo, G. Sclauzero, A. P. Seitsonen, A. Smogunov, P. Umari, R. M. Wentzcovitch, J.Phys.:Cond. Mat. **21**, 395502 (2009).

[12] J. P. Perdew and A. Zunger, Phys. Rev. B **23**, 5048 (1981).

[13] Y.-S. Lee, M. B. Nardelli, and N. Marzari, Phys. Rev. Lett. **95**, 076804 (2005).

[14] C. Bena and G. Montambaux, New J. Phys. **11**, 095003 (2009).

[15] F. Bonaccorso, Z. Sun, T. Hasan and A. C. Ferrari, Nature Photonics **4**, 611 (2010).

[16] J. L. McChesney, A. Bostwick, T. Ohta, T. Seyller, K. Horn, J. González, and E. Rotenberg, Phys. Rev. Lett. **104**, 136803 (2010).

[17] Rahul Nandkishore, and Andrey V. Chubukov, Phys. Rev. B **86**, 115426 (2012);

[18] M. L. Kiesel, C. Platt, W. Hanke, D. A. Abanin, and R. Thomale, Phys. Rev. B **86**, 020507(R) (2012).

[19] J. Gonzalez, F. Guinea, and M. A. H. Vozmediano, Phys. Rev. B 59, R2474 (1999); Phys. Rev. Lett. **77** 3589 (1996); Nucl. Phys. B **424**, 595 (1994); J. Low. Temp. Phys. **99**, 287 (1994). M. A. H. Vozmediano, M. P. Lopez-Sancho, T. Stauber, and F. Guinea, Phys. Rev. B **72**, 155121 (2005); F. Guinea, A.H. Castro Neto, and N.M.R. Peres, Eur. Phys. J. Special Topics **148**, 117 (2007).

[20] Y. Barlas, T. Pereg-Barnea, M. Polini, R. Asgari, and A. H. Mac-Donald, Phys. Rev. Lett. **98**, 236601 (2007); G. Borghi, M. Polini, R. Asgari and A. H. MacDonald, Solid State Comm. **149** 1117 (2009); A. Principi, M. Polini, R. Asgari, and A.H. MacDonald, Solid State Comm. **152**, 1456 (2012).

[21] J. Jung and A. H. MacDonald, Phys. Rev. B **84**, 085446 (2011).

[22] D.C. Elias, R.V. Gorbachev, A.S. Mayorov, A.A. Zhukov, P. Blake, L.A. Ponomarenko, I.V. Grigorieva, K.S. Novoselov, F. Guinea, and A.K. Geim, Nature Physics, **7**, 701 (2011).

[23] J. Lischner, D. Vigil-Fowler, and S. G. Louie, Phys. Rev. Lett. 110, 146801 (2013).

[24] A. Bostwick, F. Speck, T. Seyller, K. Horn, M. Polini, R. Asgari, A. H. MacDonald, E. Rotenberg, Science **328** 999 (2010); A. L. Walter, A. Bostwick, K.-J. Jeon, F. Speck, M. Ostler, T. Seyller, L. Moreschini, Y. J. Chang, M. Polini, R. Asgari, A. H. MacDonald, K. Horn, and E. Rotenberg, Phys. Rev. B 84, 085410 (2011).

[25] P. Poncharal, A. Ayari, T. Michel, and J.-L. Sauvajol, Phys. Rev. B **78**, 113407 (2008).

[26] S. Shallcross, S. Sharma, E. Kandelaki, and O. A. Pankratov, Phys. Rev. B **81**, 165105 (2010).

[27] Z. F. Wang, Feng Liu, and M. Y. Chou, Nano Lett., **12**, 3833 (2012).

[28] C. R. Dean, A. F. Young, I. Meric, C. Lee, L. Wang, S. Sorgenfrei, K. Watanabe, T. Taniguchi, P. Kim, K. L. Shepard and J. Hone, Nature Nanotech. **5**, 722 (2010).